PAPER • **OPEN ACCESS**

Ultrathin Y_2O_3:Eu^{3+}nanodiscs: spectroscopic investigations and evidence for reduced concentration quenching

To cite this article: D den Engelsen *et al* 2018 *Nanotechnology* **29** 455703

OPEN ACCESS
IOP Publishing
Nanotechnology

Nanotechnology **29** (2018) 455703 (14pp)
https://doi.org/10.1088/1361-6528/aadc83

Ultrathin Y_2O_3:Eu^{3+} nanodiscs: spectroscopic investigations and evidence for reduced concentration quenching

D den Engelsen[1], G R Fern[1], T G Ireland[1], D Hudry[2,3], A M M Abeykoon[4], D Nykypanchuk[5], J H Dickerson[2,5] and J Silver[1]

[1] Centre for Phosphor and Display Materials, Wolfson Centre for Materials Processing, Brunel University London, Uxbridge, Middlesex, UB8 3PH, United Kingdom
[2] Department of Physics, Brown University, Providence, RI 02912, United States of America
[3] Institute of Microstructure Technology, Karlsruhe Institute of Technology, Herman-von-Helmholtz-Platz 1, D-76344, Eggenstein-Leopoldshafen, Germany
[4] Photon Sciences Directorate, Brookhaven National Laboratory, Upton, NY 11973, United States of America
[5] Center for Functional Nanomaterials, Brookhaven National Laboratory, Upton, NY 11973, United States of America

E-mail: jack.silver@brunel.ac.uk

Received 25 May 2018, revised 6 August 2018
Accepted for publication 23 August 2018
Published 7 September 2018

Abstract

Here, we report the synthesis and spectral properties of ultrathin nanodiscs (NDs) of Y_2O_3:Eu^{3+}. It was found that the NDs of Y_2O_3:Eu^{3+} with a thickness of about 1 nm can be fabricated in a reproducible, facile and self-assembling process, which does not depend on the Eu^{3+} concentration. The thickness and morphology of these NDs were determined with small angle x-ray scattering and transmission electron microscopy. We found that the crystal field in these nanoparticles deviates from both the cubic and monoclinic characteristics, albeit the shape of the $^5D_0 \rightarrow {}^7F_J$ ($J = 0, 1, 2$) transitions shows some similarity with the transitions in the monoclinic material. The Raman spectra of the non-annealed NDs manifest various vibration modes of the oleic acid molecules, which are used to stabilise the NDs. The annealed NDs show two very weak Raman lines, which may be assigned to vibrational modes of Y_2O_3 NDs. The concentration quenching of the Eu^{3+} luminescence of the NDs before annealing is largely suppressed and might be explained in terms of a reduction of the phonon density of states.

Supplementary material for this article is available online

Keywords: nanodiscs, europium-doped yttrium oxide, luminescence, small angle x-ray scattering, transmission electron microscopy, Raman spectroscopy, concentration quenching

(Some figures may appear in colour only in the online journal)

1. Introduction

Rare earth-doped inorganic nanocrystals (NCs) have emerged as an intensively studied class of optically active materials [1]. Indeed, their corresponding up- and down-converting properties are of major technological interest in fields as diverse as solid-state lightning, energy harvesting, photocatalysis, and biomedical imaging [2]. The up- and down-converting properties of lanthanides (Ln) are due to electronic transitions within the 4f orbitals [3–5]. Because of the strongly localised character of the 4f electrons, Ln-based NCs do not exhibit traditional quantum confinement effects, contrary to what is usually observed for

semiconductor NCs (a.k.a. quantum dots) [4]. Although the electronic energy levels of Ln ions in NCs are not modified because of quantum confinement, size effects in these materials are nonetheless important. Indeed, the limited size of a NC, in which optically active Ln ions are embedded, can modify the spectroscopic properties and luminescent dynamics of these ions. First, reduced geometrical dimensions can affect the crystal structure of the host of the lanthanide ions [6]. Depending on the magnitude of these modifications, the site symmetry of the optically active centres can be considerably different from what is expected for their corresponding bulk counterparts. Since the site symmetry of Ln ions is of prime importance when considering electronic transitions (selection rules), this aspect must be carefully evaluated when considering Ln-based NCs. Second, electron–phonon interactions in Ln-based NCs are important because the relaxation pathways and energy transfer processes can be affected. In particular, the electron–phonon interaction is directly influenced by the phonon density of states (PDOS), which determines largely the slow-down of the decay-rate in NCs of Y_2O_3:Er^{3+} according to Chen *et al* [7]. These authors show that the energy transfer from excited Er^{3+} ions is reduced due to discretization of the PDOS in Y_2O_3 and cutting off low frequency vibrational modes in the nanosized crystals. A good understanding of these phenomena is crucial to the design and synthesis of innovative and functional, Ln-based, nanoscale building blocks of technological interest.

The spectroscopic properties of nanosized Y_2O_3:Eu^{3+} phosphor particles have been widely studied: most refer to spherical NCs or nanodiscs (NDs) thicker than 2 nm [8–13]. Wang *et al* [8] found a substantial broadening of the peaks in the spectrum of NDs of Y_2O_3:Eu^{3+} with a height of 2 nm. Zhang *et al* [9] indicated that spherical NCs with a diameter $\leqslant$5 nm show a substantial change in their photoluminescence (PL) compared to bulk material. Bazzi *et al* [10] found less broadening in spherical nanoparticles with a diameter of 3–4 nm; in their spectra three components can be distinguished in both the $^5D_0 \rightarrow {}^7F_1$ and $^5D_0 \rightarrow {}^7F_2$ manifolds. In a second paper [11] these authors presented somewhat larger line broadening of spherical NCs of about 5 nm. Moreover, they reported that the concentration quenching in 5 nm spherical NCs of Y_2O_3:Eu^{3+} is largely suppressed. Bazzi *et al* attributed this reduction to a lower energy transfer rate from the luminescence centres to the quenching centres due to the interfaces. This could be in line with the findings of Chen *et al* [7] on electron–phonon interaction; however, this possibility was not mentioned by Bazzi *et al* Pinna *et al* [12] synthesised very thin lamellae of Y_2O_3:Eu^{3+} with a thickness of about 0.5 nm. These authors did not present an explanation of the peak broadening upon reducing the thickness of the crystals to sub-nanometre sizes and they did not comment either on the spectral changes caused by annealing their lamellae that were stabilised by organic molecules. Si *et al* [13] described the synthesis of NDs made of Ln_2O_3, where Ln is one of the lanthanides (not Ce and Pm), and Y_2O_3:Eu. With their synthesis method they were able to make nanoplates and NDs with a thickness that ranged from 5 to 30 nm; they reported that line broadening starts in the NDs of Y_2O_3:Eu^{3+} that had a height of 23 nm, which is larger than found by the other authors.

The controlled synthesis of well-defined NCs of Ln oxide is challenging. Over the past two decades, several authors have reported the synthesis of europium-doped yttrium oxide NCs [8–19]. However, few have reasonable claims to have fabricated well-defined, monodisperse and crystalline nanomaterials [8, 10, 13]. From the data in the literature mentioned above, the actual line broadening and shape of the spectra of Y_2O_3:Eu^{3+} NCs can be concluded to depend on both the synthesis method and the stabilising compounds used. In spite of the electron–phonon description on the decay mechanism for NCs, published by Chen *et al* [7], a theory does not exist that predicts the changes of a spectrum of rare earth-doped material in going from a micrometre-sized powder to NCs. The objective of the present investigation is to focus on this not-so-well known field of inorganic luminescent materials.

In this paper, we report the formation, characterisation and spectral analysis of highly monodisperse and naturally self-assembled ultrathin, less than 1 nm, europium-doped yttrium oxide NDs. This synthesis method has been developed recently for pure europium oxide nanoplatelets [20].

2. Experimental details

2.1. Chemicals

Europium acetate hydrate (99.9%), yttrium acetate hydrate (99.9%) trioctylamine (N(Oct)3, 98%), oleic acid (OA, technical grade, 90%), Oleylamine (OAm, technical grade 80%–90%), absolute ethanol, toluene and n-hexane were purchased from Aldrich and were used without further purification.

2.2. Synthesis of europium-doped (5 mol%) yttrium oxide NDs

The synthesis was performed using air-free techniques under purified (5.0) nitrogen (N_2). First, $Eu(CH_3COO)_3.xH_2O$ (0.03 mmol) and $Y(CH_3COO)_3.xH_2O$ (0.57 mmol) were introduced in a mixture of $N(Oct)_3$ (6 mmol) and OA (6 mmol). The resulting mixture was heated up to 125 °C–135 °C under vigorous N_2 flow in order to dissolve $Eu(CH_3COO)_3.xH_2O$ and $Y(CH_3COO)_3.xH_2O$. The white turbid solution turned to an optically clear and slightly yellowish solution within few minutes when the temperature of the flask was >120 °C. After 20 min, the temperature was decreased to 100 °C and OAm (12 mmol) was added before vacuum purification. The latter consisted in five N_2/vacuum (1.5×10^{-2} mbar) cycles followed by a dynamic vacuum (5×10^{-3} mbar) for 10 min. Finally, glacial acetic acid (1.5 mmol) was added. The resulting mixture was heated up (10 °C min^{-1}) to 300 °C for 60 min. Afterwards, the heating mantle was removed and the flask was left to cool naturally to room temperature. All details regarding the experimental setup can be found in [20].

The same procedure was applied for europium-doped yttrium oxide NDs with other Eu contents as the one described above. The total quantity of Eu and Y was maintained at 0.6 mmol.

2.3. NCs recovery and purification procedure

Absolute ethanol was added (at room temperature) to the thermally treated solution. The solution flocculated immediately. After centrifuging (3500 rpm, 1 min) the clear supernatant was discarded and the resulting white precipitate was dispersed in toluene. A highly opalescent solution was obtained instead of an optically clear solution. While highly opalescent, no remaining powder remains in suspension, and no powdery precipitate was observed with time. This purification procedure (ethanol precipitation, centrifuging, toluene dispersion) was repeated three times to remove all residual organics. After an ultimate centrifuging step, the white precipitate was dried under vacuum. This white powder was characterised and measured with the organic stabilising materials adsorbed to the surface; however, we also annealed the NDs at 500 °C in air to get rid of the organic matter and study what happened to the NDs.

2.4. Transmission electron microscopy (TEM)

Low resolution TEM analyses of europium oxide NCs were conducted with a JEOL 1400 operating at 120 kV and equipped with a Gatan CCD camera for imaging. TEM samples were prepared by drop-casting (10 μl) diluted suspensions of the NCs in toluene or methanol onto ultrathin carbon coated copper grids. No special conditions were used to control the toluene or methanol evaporation. Some samples were investigated in the TEM of Brunel University (JEOL 2100 F, operating at 200 kV), which was equipped with a Gatan Vulcan cathodoluminescence (CL) detector for imaging and spectroscopic purposes. This system used a Czerny–Turner spectrometer with back-illuminated CCD and gratings with 1200 or 2400 grooves per mm for collection of CL emission spectra. Light was collected from the sample using a mirror above and below the sample, which enabled a solid angle of about 5 Sr, which is almost half of a sphere. This high solid angle made light collection highly efficient and enabled the collection of CL at low intensity. A small cryostat connected to the sample holder enabled cooling of the samples in the TEM down to 103 K (−170 °C); adjustment of the sample temperature anywhere between 103 K and 303 K was facile.

CL-spectra were recorded with a defocussed e-beam, spot size ~5 μm. This method was preferred to suppress e-beam damage of the NDs. In order to get sufficient luminescence, the specimens had to be thicker than 200 nm, preferably >1 μm, and the area from which the luminescence was collected must be larger than 1 μm as well. Thus, a rather large area of the sample was excited which impeded the collection of CL-spectra from individual NDs (using a focussed e-beam).

2.5. SAXS measurements

Small angle x-ray scattering (SAXS) measurements were conducted on a Bruker Nanostar U instrument equipped with rotating Cu anode and VANTEC 2000 2D detector. The sample-to-detector distance was calibrated using Silver Behenate as a standard. Solution based measurements were done in sealed 1 mm glass capillaries (Charles Supper, MA) while dried samples were measured in 1 mm inner diameter Kapton capillaries. SAXS modelling was done using the Irena software package [21].

2.6. Spectroscopic measurements

All spectroscopic measurements were performed on the dried samples. The PL excitation and emission spectra of the samples were collected using a Bentham phosphor spectrometer system (Bentham Instruments Ltd, Reading, UK), configured with M300 excitation and emission monochromators, to which the emission monochromator was mounted an IL7D modular xenon light source (150 W) connected to the measuring chamber via a fibre optic bundle. Excitation wavelengths 267, 395 and 465 nm were used for emission spectra, the excitation spectra were measured monitoring the 613 nm emission peak.

Laser-induced fluorescence spectra of the samples were measured with a Horiba Jobin Yvon Labram HR monochromator by excitation with a He–Ne laser at various temperatures. The wavelength error of the Labram monochromator was smaller than ±0.02 nm. Transmission filters (10% and 25%) were used to vary the excitation power of the He–Ne laser. Upon stepping from one temperature to another the effects of temperature drift had to be nullified. This was done by monitoring the position of the laser spot on the sample by a microscope and careful manual readjustment using the automated microscope stage focussed on a prominent surface feature as a marker. The spectra were recorded over a temperature range from −200 °C to 200 °C in steps of 25 °C or 50 °C using a THMS600 heating and cooling stage, which was controlled by a TMS94 temperature controller with a temperature accuracy of ±0.1 °C.

2.7. PDF and WAXS measurements

X-ray atomic pair distribution function (PDF) and medium resolution wide angle x-ray scattering (WAXS) measurements were carried out at the X17A beamline at the National Synchrotron Light Source (NSLS) at Brookhaven National Laboratory. The dried samples were inserted into 1 mm inner diameter Kapton capillaries. These were sealed with clay. Measurements were performed in capillary transmission geometry using a (0.5 × 0.5) mm^2 monochromatic (67 keV; $\lambda = 0.186$ Å) x-ray beam. Two PerkinElmer amorphous silicon area detectors, mounted orthogonal to the beam path were used for data collection. PDF measurements were carried out using the front detector at the sample-to-detector distance 204 mm. WAXS measurements were carried out using the far detector at the sample-to-detector distance, 1517 mm.

Table 1. Sample identification and the corresponding elementary chemical composition of the as-prepared europium-doped yttrium oxide NDs synthesised by the thermal decomposition of europium and yttrium acetates in a mixture of oleic acid, tri-n-octylamine, oleylamine and acetic acid. The initial content refers to the starting quantities of yttrium and europium used for the synthesis (calculated from the mass of each acetate precursor). The final content refers to the final quantities of yttrium and europium found in the extracted, purified, and dried NDs, as determined by ICP-AES.

	Initial content/mol%		Final content/mol%	
Sample ID	Y	Eu	Y	Eu
S00	100	0	100	BDL*
S05	95	5	95.5	4.5
S10	90	10	90.4	9.6
S20	80	20	81.3	18.7
S30	70	30	71.6	28.4
S40	60	40	61.3	38.7
S50	50	50	51.9	48.1
S100	0	100	BDL*	100

Note: *BDL means beyond detectable levels.

3. Results and discussion

The Y_2O_3:Eu_{3+} NCs were prepared by the method as described above, which is similar to the one reported by Si *et al* [13], but slightly modified from the method that we recently reported for ultrathin Eu_2O_3 nanoplatelets [20]. The identification of each sample and its corresponding elementary chemical composition (yttrium and europium contents) are given in table 1. For simplicity and because the final contents of yttrium and europium determined in the as-prepared NCs are very close to the initial contents (see table 1), the samples are identified according to their starting europium content throughout the text and figures as well. TEM images for the six different Y_2O_3:Eu^{3+} NCs (samples S05–S50) are shown in figure 1. Independent of the europium content, the TEM images clearly show the formation of NDs with a mean diameter ranging from 30 to 35 nm. Note that the undoped sample (S0) is characterised by the formation of similar NDs (figure S1, which is available online at stacks.iop.org/NANO/29/455703/mmedia), whereas the sample only made of europium (S100) is characterised by the formation of ultrathin square nanoplatelets (figure S2) [20] with a thickness of also 1 nm. Interestingly, all of the as-prepared NDs are highly anisotropic with a constant and ultrathin thickness as small as 0.9 ± 0.2 nm (figure S3(a)).

Another interesting feature of the as-prepared NDs is their natural capacity to self-assemble into long fibre-like superstructures with lengths ranging from several hundred of nanometres (figure 1) up to few micrometres (figure S3(b)). The possible self-assembly of NCs requires a more careful look, as the phenomena can potentially affect both synthetic steps as well as optical properties.

Figure 1(d) exhibits a cylindrical shape of the NDs of Y_2O_3:Eu^{3+}, whereas NDs that were annealed at 500 °C in air showed predominantly triangular NDs. Typical shapes are shown in figure 2. The formation of fibre-like superstructures

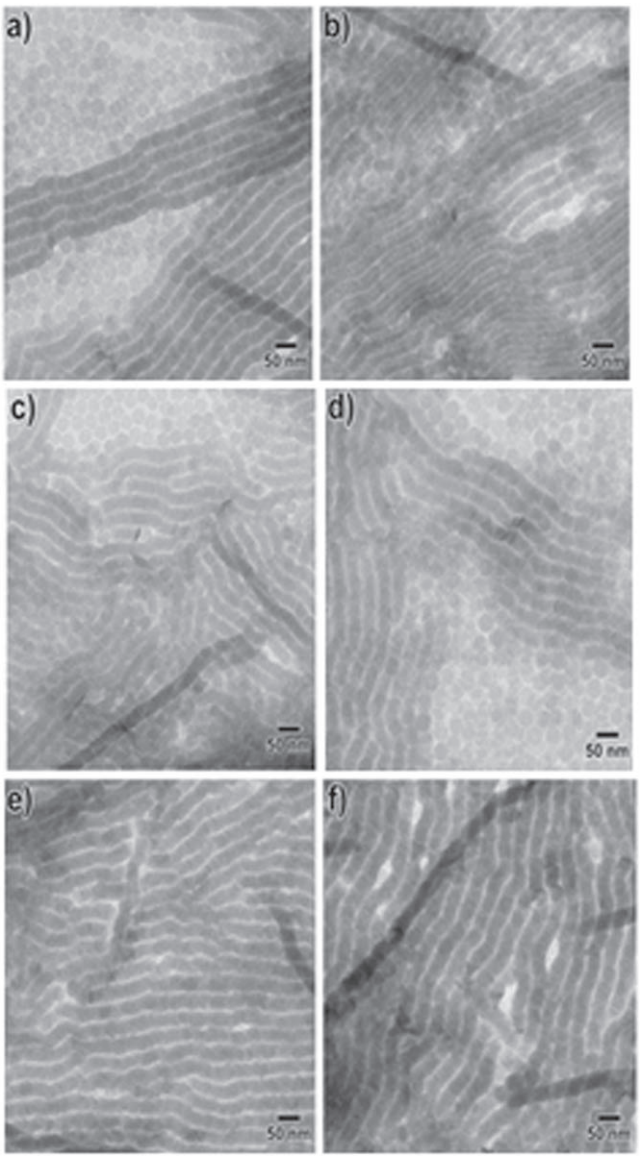

Figure 1. Low magnification TEM images of ultrathin europium-doped yttrium oxide NDs with various europium contents in mol%: (a) 5%, (b) 10%, (c) 20%, (d) 30%, (e) 40%, and (f) 50%. The NDs were prepared by the heating-up technique (310 °C–60 min) with europium and yttrium acetates initially dissolved in a mixture of oleic acid, oleylamine, tri-n-octylamine and acetic acid. The NDs naturally self-assemble into 1D fibre-like superstructures (nanoworms).

similar to those in figure 1 has been previously observed by Si *et al* [13] and Ding *et al* [22]. These authors attributed the phenomenon either to drying effects of highly monodisperse NDs when drop-casted onto a TEM grid or to the modification of the polarity of the solvent (e.g. mixture of cyclohexane and ethanol), which are not completely satisfactory explanations.

We assume, however, that self-assembly of the as-prepared NDs is an intrinsic property of the synthesis method. Substantiating evidence for this hypothesis is that the employment of sonication for up to 60 min was insufficient to prevent the self-assembly; moreover, once extracted and purified, the NDs cannot be dispersed in apolar solvents, such

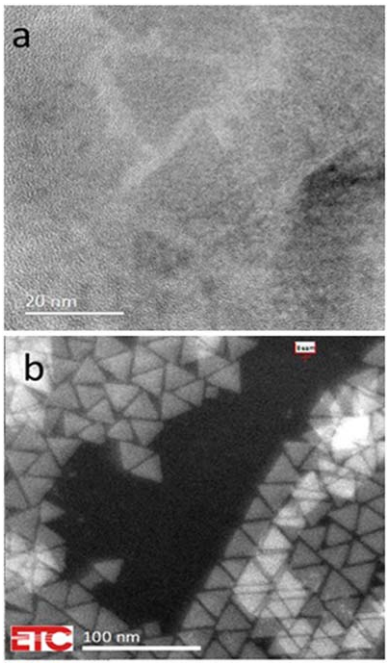

Figure 2. TEM images of S20 after annealing at 500 °C in air. From the TEM image in a it can be derived that the equilateral triangles have sides of 25 nm. (b) High-angle annular dark-field image showing how the triangles cover the area.

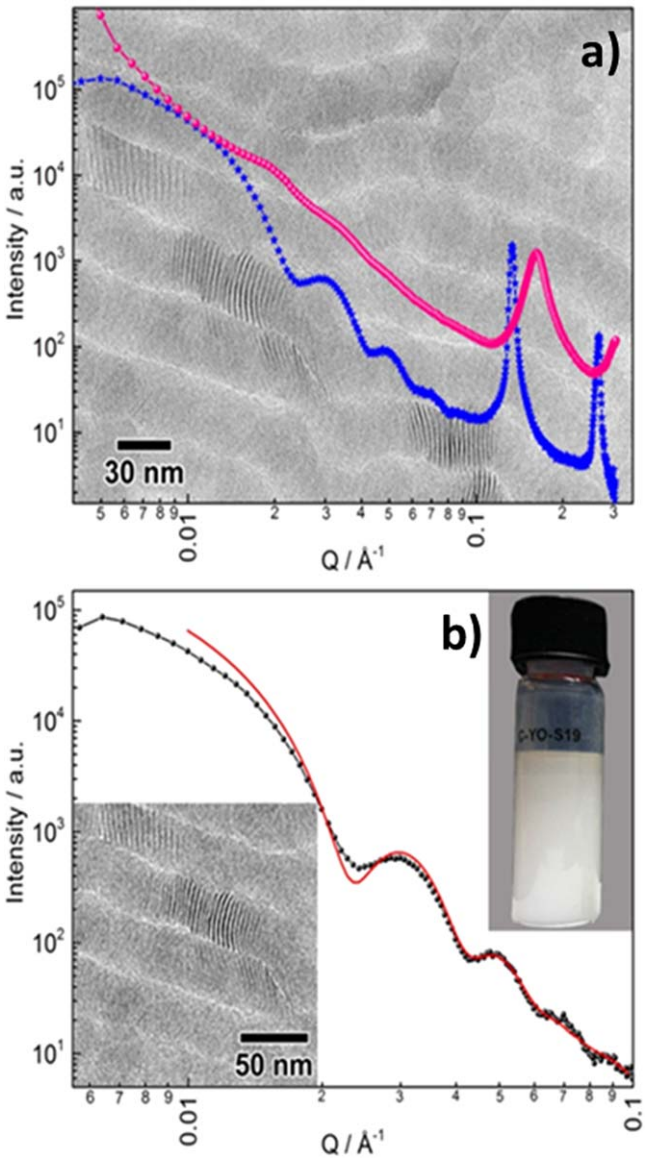

Figure 3. (a) SAXS data of S20 NDs dispersed in toluene (blue stars) and the corresponding dried powder (magenta spheres). The background is a high magnification transmission electron microscopy (TEM) image of the sample drop-casted onto the TEM grid (i.e. toluene evaporation). (b) Modelling of the low Q region SAXS data for the NDs dispersed in toluene. The experimental data (black spheres) and the fit data based on the cylinder model (red line) juxtapose reasonably well. The upper right inset is a photograph of a suspension of the ultrathin NDs in toluene. The lower left inset is a high magnification TEM image showing the self-assembled NDs oriented parallel (black stripes) to the TEM incident electron beam. From this image, the inter-disc distance was calculated to compare with the SAXS inter-disc data.

as toluene or hexane. Instead of obtaining an optically clear solution, as usually is the case for NCs with similar dimensions, a strongly opalescent solution was obtained, shown in upper right inset of figure 3(b). This solution was characterised by SAXS, and the results are presented in figure 3. Clearly, the NDs are self-assembled in apolar solvents (toluene) without the need of adding polar solvents (figure 3(a), blue curve). The two peaks observed within the high Q region (0.1–0.3 Å^{-1}) are equally spaced and consistent with lamella-like arrangement of NDs seen in the TEM images. The calculated centre to centre inter-disc distance d is 4.7 nm ($d = 2\pi/q$), which is somewhat larger than what can be derived from the TEM image (3.4 nm) of a dried sample. The low Q region (0.01–0.1 Å^{-1}) is well modelled by cylindrical shapes of ∼33 nm ± 3 nm (figure 3(b)) and is in good agreement with the TEM data and corresponding cylinder-like arrangement of the NCs. Finally, once dried (i.e. powdery sample), the self-assembly persists but is clearly disturbed (figure 3(a), magenta curve) with both increasing disorder (broadening of the peaks) and modification of the inter-disc distance now equalling 3.9 nm, which is in excellent agreement with TEM data. The inter-disc spacing of 4.7 nm is two times the length of elaidic acid, which is the trans-isomer of oleic acid, whereas a spacing of 3.9 nm matches almost two times the projected distance of (cis-) oleic acid [23]. From this observation it can be concluded that the carboxylate group of the oleic acid molecules is bonded to the ND-surface and that the aliphatic chain (2x) serves as a spacer when the ND are piling up [16, 20].

The mechanism governing the self-assembly of such ultrathin NDs is currently under investigation and not entirely understood. Several authors have reported on the formation of ultrathin NCs due to the low temperature template-assisted mechanism [24–26]. In such a mechanism, the starting inorganic precursors form molecular complexes that self-assemble into ordered superstructures, which presumably ultimately act as a template within which the growth of the inorganic NCs is constrained. Although, in the case of Y_2O_3:Eu^{3+} NDs,

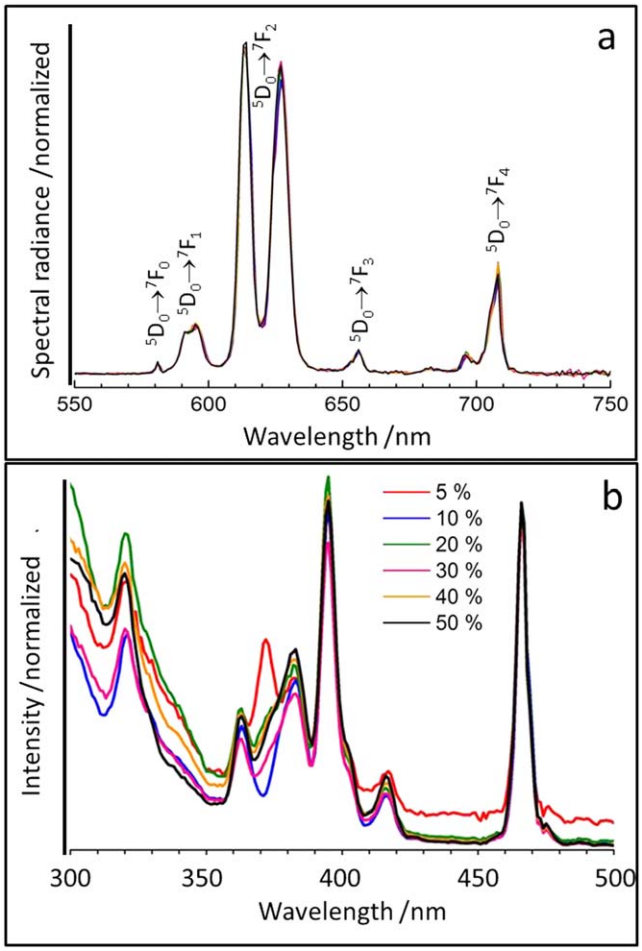

Figure 4. Overlay of PL spectra of non-annealed Y_2O_3:Eu^{3+} NDs with Eu^{3+} concentration from 5 to 50 mol%. (a) Emission spectra ($\lambda_{ex.} = 267$ nm). (b) Excitation spectra ($\lambda_{em.} = 613$ nm). The normalised emission spectra in (a) for materials with different Eu^{3+} concentration coincide.

such a mechanism cannot be completely ruled out, it is, we believe, unlikely because of the high temperature of the synthesis. Alternatively, self-assembly may be caused by preferential binding of ligands at the nucleation stage to a certain crystal plane, which may lead to anisotropic growth of the NCs. The resulting nanoplatelets can self-assemble simply due to van der Waals interactions. High temperature *in situ* SAXS experiments will be necessary to identify unambiguously the mechanism that is responsible for the self-assembly.

3.1. Spectroscopic measurements

To elucidate the effect of structure change under ultra-small confinement we investigated the luminescent properties of the ultrathin NDs with (PL), both lamp and laser-activated, and CL. First we shall describe the PL spectra excited with the Xe lamp. The normalised PL emission ($\lambda_{ex.} = 267$ nm) and excitation ($\lambda_{em.} = 613$ nm) spectra of the NDs are presented in figures 4(a) and (b), respectively. In these figures the spectra for NDs with different Eu^{3+} concentrations have been overlaid. The shape of the emission spectra does not change upon varying the Eu^{3+} concentration, while in the excitation spectra some differences can be noticed, notably for S05. All observed transitions in the emission spectra can be ascribed to the $^5D_0 \rightarrow {}^7F_J$ ($J = 0$–4) transitions. The NDs doped with 5 mol% Eu are the least efficient, while the ones doped with 40 mol% are the most efficient with a lumen efficacy of over 20 lm w^{-1} and a quantum efficiency of about 5%. Since these latter measurements were extremely difficult due to the small amount of material available, it is in fact very likely that the lumen efficacies we measured erred on the low side. The highest quantum efficiency (PL) for bulk Y_2O_3:Eu^{3+} phosphors is obtained at concentrations at about 10 mol% Eu^{3+} [27], which indicates that the NDs show a substantial reduction of the concentration quenching. This phenomenon will be discussed in detail hereafter.

Figure 5 is a collection of laser-activated (LA)-spectra of non-annealed Y_2O_3:Eu_3 + NDs with 20 mol% Eu^{3+}. For reasons of clarity the spectra for only three temperatures are shown, namely at −75 °C, (0 °C in figure 5(b)), 25 °C and 125 °C.

Figure 5(a) features besides the 5D0 → $7F_J$ ($J = 0$, 1, 2, 3 and 4) transitions of Eu^{3+} a weak band at about 775 nm, which is made up of the Raman-active vibrations of oleic acid, to be discussed hereafter. Figure 5(b) presents the $^5D_0 \rightarrow {}^7F_J$ ($J = 0$, 1, 2) electronic transitions of Eu^{3+}in the Y_2O_3:Eu^{3+} NDs. Figure 5(a) shows that the electronic transitions of Eu^{3+} are strongly temperature dependent. Silver *et al* [28] have described the LA-spectra for Y_2O_3:Eu^{3+} particles with a diameter of about 300 nm. Although this diameter indicated the nano-character of their sample, their LA-spectrum manifested still largely bulk features regarding positioning of the energy levels and widths of transitions. They indicated that the $^5D_0$ level of Eu^{3+} in cubic Y_2O_3 can be populated by the 632.8 nm irradiation of the He–Ne laser after sufficient thermal population of the $^7F_4$ level of Eu^{3+}, which implies a strong temperature dependence of the Eu^{3+} luminescence. Figure 5(c) manifests the $^5D_1 \rightarrow {}^7F_1$ and $^5D_1 \rightarrow {}^7F_2$ transition manifolds of Eu^{3+}, which cannot be observed at low temperatures. Also these transitions are substantially broadened compared to the same transitions in the LA-spectrum of bulk Y_2O_3:Eu^{3+} [28]. Hardly visible in figure 5(c) is the $^5D_1 \rightarrow {}^7F_0$ transition manifold at 527.1 nm: at 200 °C this transition is clearly noticeable. Figures 6 and 7 present the deconvolutions of the $^5D_0 \rightarrow {}^7F_1$ and $^5D_0 \rightarrow {}^7F_2$ transitions respectively, initially shown in figure 5(b).

The tables added to figures 6 and 7 present the parameters that describe the Lorentzian profiles *pi* ($i = 1$, 2, etc), where A is the amplitude (in arbitrary units), λ_0 is the wavelength at maximum spectral radiance and FWHM is the full width at half maximum.

The deconvolutions of spectra recorded at other temperatures indicate that the ratio of the amplitudes and the widths of the profiles did not change significantly and that the wavelengths at maximum spectral radiance changed only slightly. The deconvolutions of the $^5D_0 \rightarrow {}^7F_3$ and $^5D_0 \rightarrow {}^7F_4$ transitions of Eu^{3+} in Y_2O_3:Eu^{3+} NDs were less reliable due to the larger number of crystal field components. It is interesting to see that the $^5D_0 \rightarrow {}^7F_J$ ($J = 0$, 1, 2) electronic

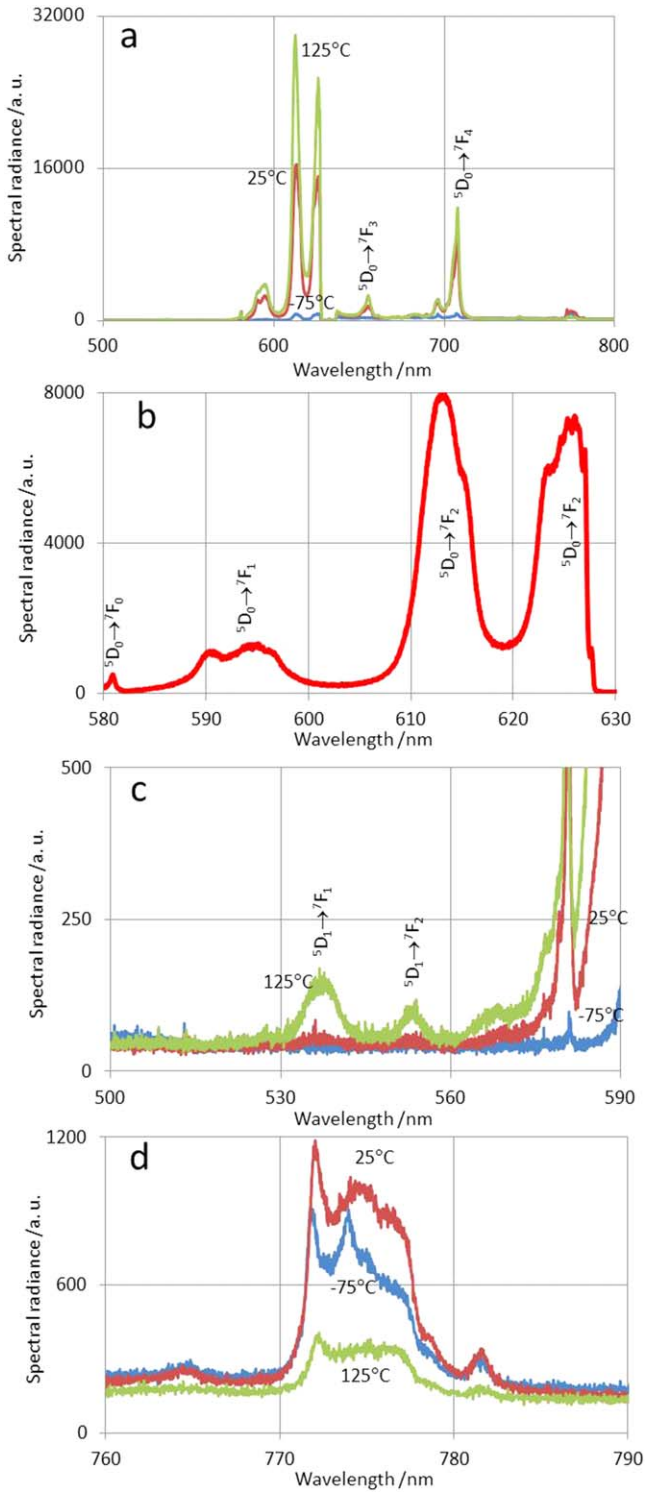

Figure 5. Laser-activated spectra of S20 at various temperatures. (a) Overview between 500 and 800 nm. The He–Ne laser line at 632.8 nm has been deleted from this spectrum. (b) Anti-Stokes spectrum between 580 and 630 nm recorded at 0 °C. (c) Anti-Stokes spectrum (magnified) between 500 and 590 nm. (d) Part of Stokes spectrum (magnified) between 760 and 790 nm.

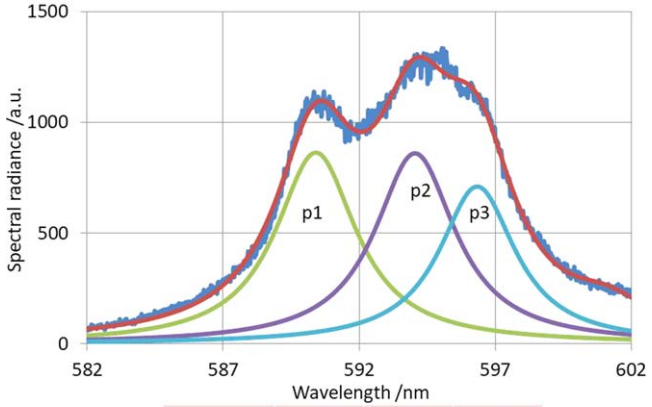

	p1	p2	p3
A	864.3	861.2	711.1
λ_0 (nm)	590.4	594.1	596.3
FWHM (nm)	3.6	3.6	3.4

Figure 6. Deconvolution of $^5D_0 \rightarrow {}^7F_1$ transitions of Eu^{3+} in S20 NDs recorded at 0 °C. Deconvolution was achieved with three Lorentzian profiles, which were fitted to the experimental spectrum with a least squares algorithm using the solver of Excel Microsoft.

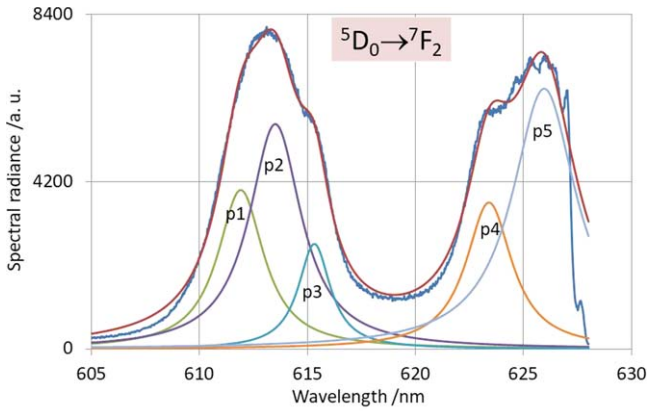

	p1	p2	p3	p4	p5
A	3993	5646	2639	3679	6536
λ_0 (nm)	611.9	613.5	615.3	623.4	626.0
FWHM (nm)	2.6	2.94	1.8	2.6	3.6

Figure 7. Deconvolution of $^5D_0 \rightarrow {}^7F_2$ transitions of Eu^{3+} in S20 NDs recorded at 0 °C. Deconvolution was achieved with five Lorentzian profiles, which were fitted to the experimental spectrum with a least squares algorithm using the solver of Microsoft Excel.

transitions of Eu^{3+} in the Y_2O_3:Eu^{3+} NDs deviate significantly from the corresponding transitions in bulk cubic Y_2O_3:Eu^{3+}, both in the height and the location of the peaks. Moreover, the peaks are substantially broadened compared to the widths of corresponding peaks from bulk material. In table 2 the electronic levels determining the $^5D_0 \rightarrow {}^7F_J$ ($J = 0, 1, 2$), $^5D_1 \rightarrow {}^7F_0$ and $^5D_1 \rightarrow {}^7F_1$ manifolds of Y_2O_3:Eu^{3+} are listed for cubic bulk material and the NDs.

Table 2 indicates that the Eu^{3+} cation sites in Y_2O_3:Eu^{3+} NDs have a different electrostatic environments from those in Y_2O_3:Eu^{3+} itself, which leads to different Stark splitting. Table 2 does not contain the corresponding levels for monoclinic bulk Y_2O_3:Eu^{3+}, because the assignment of the transitions of Eu^{3+} in the three cation sites of the monoclinic phase is incomplete [30, 31]. Figure 8 presents a comparison of the LA-spectra of monoclinic and cubic Y_2O_3:2%Eu^{3+} particles and NDs of S05, non-annealed and annealed at 500 °C. The monoclinic particles had crystallites of about

Table 2. Energy levels (in cm^{-1}) of lowest ^7F_J, $^5D_0$ and $^5D_1$ states of ND and cubic bulk Y_2O_3:Eu^{3+}.

Level	ND	Bulk [29]
$^7F_0$	0	0
	277	199
$^7F_1$	390	360
	450	543
$^7F_2$	874	859
	916	906
	964	949
	1175	
	1240	1380
$^7F_3$	1949[a]	2017[b]
$^7F_4$	3084[a]	3005[b]
$^5D_0$	17 216	17 216
$^5D_1$	18 971	18 930
		18 954
		18 992

[a] Level of highest peak.
[b] Centroid level.

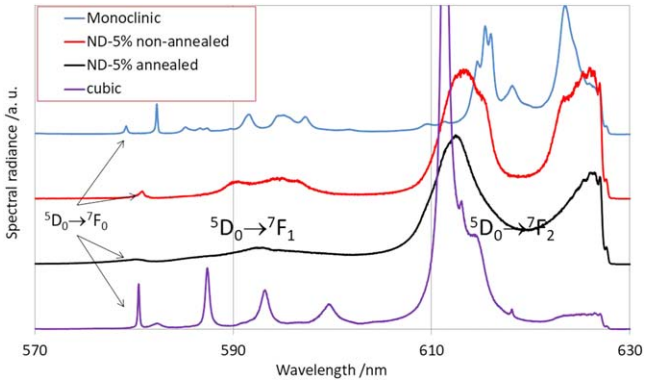

Figure 8. LA-spectra (He–Ne laser) of monclinic and cubic Y_2O_3:2%Eu^{3+} particles and NDs of S05, both non-annealed and annealed. All spectra were recorded at 25 °C. The synthesis of the monoclinic material has been described previously [30].

18 nm, while the cubic particles consisted of crystallites of about 45 nm [30].

The Stark splittings of the $^5D_0 \rightarrow {}^7F_J$ ($J = 1, 2$) multiplets of the NDs and the monoclinic and cubic materials in figure 8 differ greatly from each other, which proves that the crystal structure of the NDs is neither cubic, nor a monoclinic. Since it is impossible to determine the crystal structure from the Stark splittings, as illustrated in figures 6–8 and table 2, only qualitative conclusions can be drawn.

The correspondence between the non-annealed NDs and the monoclinic material is visually better than between the NDs and cubic Y_2O_3:Eu^{3+} because of the dominance of the 611 nm peak in the cubic material. Figure 8 also clearly illustrates the peak broadening of the NDs. Table 2 and figure 8 both support the conclusion that the Eu^{3+} sites in Y_2O_3-NDs (and most likely the Y^{3+} sites) are deviating more from the Eu^{3+} sites in cubic Y_2O_3 than from those in monoclinic Y_2O_3. It is worth noting that there are three

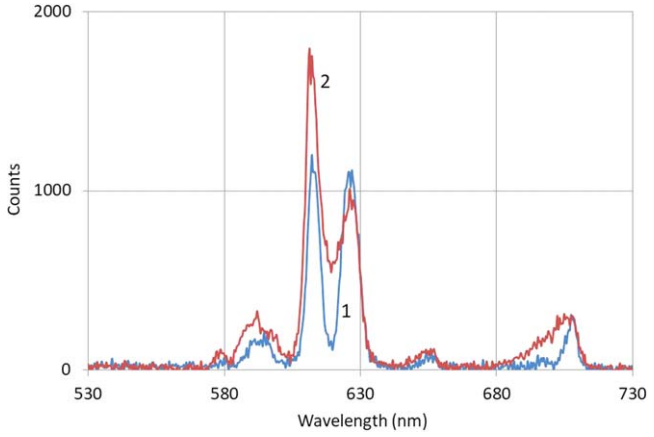

Figure 9. CL-spectra of S20 NDs recorded at −169.5 °C and 200 keV in the TEM. Spectrum 1: non-annealed NDs; spectrum 2: NDs annealed at 500 °C.

different crystallographic cation sites in monoclinic Y_2O_3 [31]. Thus, one can reasonably assume that the Y_2O_3:Eu^{3+}-NDs also contain at least two (cubic) or three (monoclinic) different Eu^{3+} crystallographic sites. In table 2 the energy levels for only one site are presented: if three sites indeed exist, two of these have a low occupancy and do not yield spectroscopic earmarks. By annealing at 500 °C not only the Raman spectra of the stabilising organic compounds disappear, but also the electrostatic environment of the Eu^{3+} ions changes slightly. The differences between the two ND-spectra in figure 8 refer to the ratio between the peaks at 613 and 627 nm, and to the shape of the $^5D_0 \rightarrow {}^7F_1$ manifold at 594 nm. The effect of annealing was also observed by CL of the NDs; this is shown in figure 9.

The same trend for the annealing effect as in figure 8 can be observed in figure 9: the ratio between the peak heights at 626 and 613 nm decreases upon annealing. It is as if the NDs get more cubic-like properties by this annealing process.

The analyses presented herein refer largely to the non-annealed samples, which have the adsorbed stabilising organic materials; later in this discussion we shall return to the annealed samples.

A characteristic feature of the spectra presented in figures 5 and 8 is the broadening of the Eu^{3+} transitions. This phenomenon has been observed by other scientists in Y_2O_3:Eu^{3+} NCs of various shapes [8–13]. Zhang *et al* [9] indicated that spherical NCs with a diameter $\leqslant$5 nm show a substantial change of the PL. These authors also suggested that the peak at 622 nm in their spectrum (corresponding to the p4-peak in figure 5) can be linked to the luminescence of Eu^{3+} in a surface state. Pinna *et al* [12] synthesised very thin lamellae of Y_2O_3:Eu^{3+} with a thickness of about 0.5 nm. The spectra of these lamellae are similar to the spectra presented in figures 3, 4 and 7: Pinna *et al* also found a change of the ratio between the peaks at 613 and 627 nm after annealing at 550 °C. None of these authors presented an explanation for the peak broadening upon decreasing the size of the crystals, while Pinna *et al* [12] did not comment on the spectral changes by annealing. Finally, Si *et al* [13] found that line

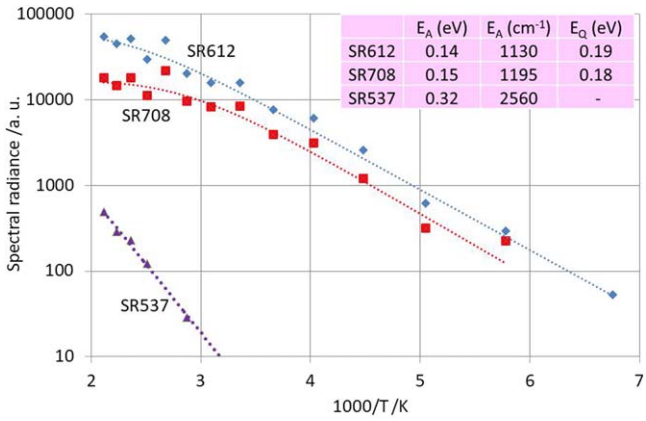

Figure 10. Arrhenius plot of spectral radiance of 537, 612 and 708 nm transitions of Y_2O_3:20%Eu^{3+} ND sample. Dotted lines according to equation (1) have been fitted to the experimental data. The activation and quenching energies are indicated in the insert.

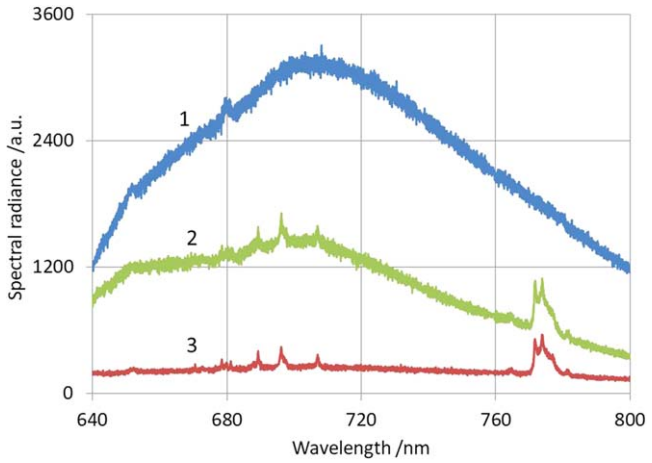

Figure 11. Low temperature spectra of three ND samples. Spectrum 1: S05 NDs annealed at 500 °C recorded at −150 °C; spectrum 2: S20 NDs recorded at −200 °C; spectrum 3: S05 NDs recorded at −195 °C.

broadening occurs in NDs of Y_2O_3:Eu^{3+} with a thickness of 23 nm, which is larger than found by the other authors. From the data in the literature discussed above, the actual line broadening and shape of the spectra likely depend on the synthesis method and the stabilising compounds.

Figure 10 depicts Arrhenius plots of the spectral radiance of the $^5D_1 \rightarrow {}^7F_2$ (537 nm), $^5D_0 \rightarrow {}^7F_2$ (612 nm) and $^5D_0 \rightarrow {}^7F_4$ (708 nm) transitions manifolds of the Y_2O_3:20%Eu^{3+} ND sample. The dotted curves in figure 10 have been fitted to:

$$\mathrm{SR}(T) = \frac{P\mathrm{e}^{-E_\mathrm{A}/kT}}{(1 + B\mathrm{e}^{-E_\mathrm{Q}/kT})}, \qquad (1)$$

where P is a pre-exponential factor, E_A is the activation energy, k is Boltzmann's constant, T is the absolute temperature, B is the pre-exponential factor in the denominator and E_Q is the quenching energy barrier [32]. The nominator of equation (1) describes the low temperature side of the curves in figure 10, while the denominator describes the quenching (a single barrier model) at high temperatures.

Due to temperature quenching the curves for SR612 and SR708 show some levelling off. The data for SR537 are limited and do not show levelling off: the dotted line for SR537 was therefore fitted by setting $B = 0$. The presence of the $^5D_0 \rightarrow {}^7F_0$, $^5D_0 \rightarrow {}^7F_1$ and $^5D_0 \rightarrow {}^7F_2$ transitions in figure 8 requires that the $^5D_0$ level of Eu^{3+} is populated by the He–Ne laser. This can be achieved by a two-photon absorption process; however, such a process is not expected to be temperature dependent. The other possibility is thermal population of the ^7F_J levels and then absorption of a He–Ne photon (15 803 cm^{-1}) to reach the actual ^5D_J level, in which $J = 0$ for the transitions mentioned above and $J = 1$ for the $^5D_1 \rightarrow {}^7F_1$ manifold (SR537). From table 2 it can be derived that we need 1413 cm^{-1} to populate the $^5D_0$ level with the He–Ne laser, which is larger than the E_A-values derived from the Arrhenius analysis represented in figure 10. The activation energy for the $^5D_1 \rightarrow {}^7F_1$ transition is found to be 2560 cm^{-1}, which is not sufficient to populate the $^5D_1$ level with one He–Ne photon: this would require 3168 cm^{-1} (table 2). It should be kept in mind that activation energies determined in this way are average values. Although the obtained values are smaller than those obtained from the spectral transitions, the Boltzmann factor guarantees sufficient population of the $^5D_0$ and $^5D_0$ levels. As indicated by Silver *et al* [27], the Arrhenius-type analysis presented here is sensitive to experimental errors. They also mentioned that cross relaxation processes may lower the activation energy determined by the Arrhenius-type analysis.

We shall now consider the Raman lines, such as the transition cluster at 773 nm in figure 5(d), in the spectra. Figure 11 presents low temperature spectra of three different ND samples.

At temperatures <-150 °C, Eu^{3+} cannot be excited by the He–Ne laser, and we can only observe Raman-active transitions, as seen in figure 11. By annealing the NDs at 500 °C the adsorbed/co-ordinated organic compounds (oleic acid, tri-n-octylamine and Oleylamine) presumably disappear completely. In table 3 we have summarised the observed Raman-active lines of figure 11.

Evidenced from figure 11 and table 3 two (very) weak Raman lines exist with shifts of 1075 and 442 cm^{-1} that cannot be assigned to the stabilising organic compounds. The vibrational modes of the NDs could be responsible for these two weak lines; yet, the Raman shifts of these lines have no relation to the Raman spectra of cubic and monoclinic Y_2O_3 [30, 31]. *A fortiori*, by comparing spectrum 1 with the Raman spectrum (Stokes side) of monoclinic Y_2O_3:2%Eu^{2+} with its 14 much stronger Raman lines, such an assignment is not particularly obvious. Nevertheless, by assigning these Raman lines to vibration modes of the ND, it can be concluded that the electron–phonon interaction in Y_2O_3:Eu^{3+} NDs is weak. This conclusion is even more convincing if the 1075 and 442 cm^{-1} lines of spectrum 1 in figure 11 are not due to ND-vibrational modes.

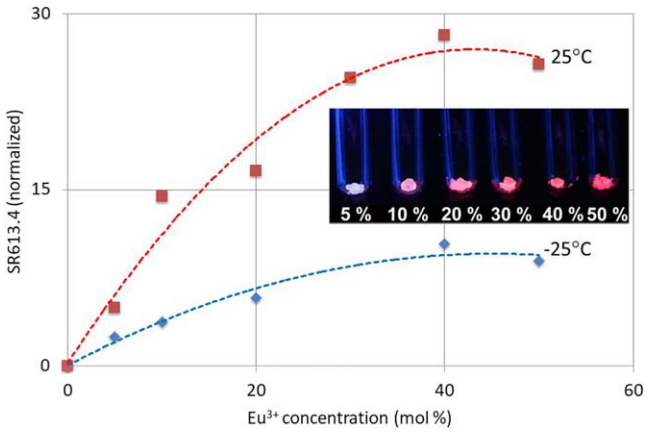

Figure 12. Normalised spectral radiance versus Eu^{3+} doping concentration. SR613.4 stands for spectral radiance at 613.4 nm, represented here for the measurements at −25 °C and 25 °C. Curves are polynomial fits through the experimental points. The insert is a photograph of the Y_2O_3:Eu^{3+} NDs under 365 nm UV light.

Table 3. Raman lines observed in figure 10.

Obs. (nm)	Obs. (cm^{-1})	Raman shift (cm^{-1})	Assignment[a]	References
781.4	12 798	3005	organic	
773.8	12 923	2880	OA: 2911 C–H	[16]
771.7	12 958	2844	OA: 2866 C Raman lines observed inH	[16]
764.2	13 086	2717	organic	
707	14 144	1659	OA: 1715 C=O	[16]
696.2	14 364	1439	OA: 1448 COO	[16]
689.3	14 507	1295	organic	
679	14 728	1075	ND?	
651	15 361	442	ND?	

[a] OA = Oleic acid.

Figure 12 presents the spectral radiance of the $^5D_0 \rightarrow {}^7F_2$ transition of Eu^{3+} in Y_2O_3:Eu^{3+} NDs with various Eu^{3+} concentrations at −25 °C and 25 °C. This spectral radiance has been normalised to the peak height of the Raman line at 772.0 nm. This normalisation reduced the spread in the data considerably, because it is assumed that the quantity of adsorbed oleic acid is constant for NDs with varying amounts of Eu^{3+}.

Figure 12 shows that the spectral radiance reaches a plateau at about 40 mol% Eu^{3+}. This is a surprising result, because concentration quenching in bulk cubic Y_2O_3:Eu^{3+} establishes the maximum efficiency at about 2 mol% Eu^{3+} for CL [33] and at about 10 mol% Eu^{3+} [27] for PL. In other words, the concentration quenching in Y_2O_3:Eu^{3+} ND begins at approximately four times larger Eu^{3+} concentration in the PL-based data of figure 12. Bazzi *et al* [11] found also that the concentration quenching in 5 nm spherical NCs of Y_2O_3:Eu^{3+} is largely suppressed. They attributed this reduction to a lower energy transfer rate from the luminescence centres to the quenching centres due to the interfaces. Although it will be difficult to disagree with this idea, it remains a little too generic, since the mechanism was not specified by them.

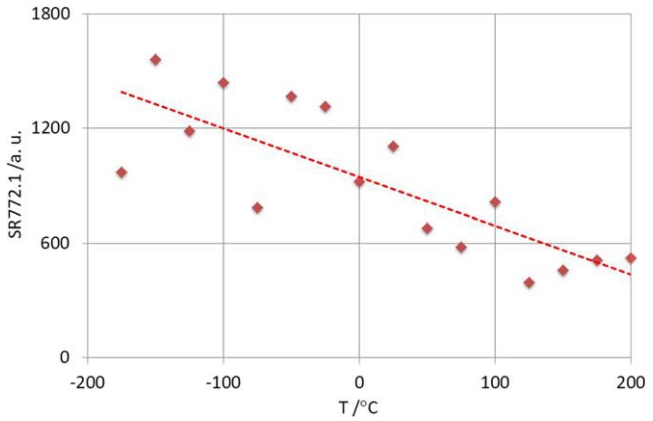

Figure 13. Spectral radiance of CH-vibration band at 772.1 nm versus temperature. Sample: S20 NDs, non-annealed. The dashed line represents the trend of the experimental points.

Figure 13 shows that the spectral radiance of the Raman-active C–H vibration band is also temperature dependant; it varies by almost a factor of 3 from −200 °C to 200 °C. For Y_2O_3:Eu^{3+} NDs with other Eu^{3+} concentrations, a similar temperature dependence of the C–H vibration band was found. It can be concluded from figure 13 that the Raman-active vibrations of oleic acid show an opposite temperature behaviour compared to the Eu-based transitions in the LA-spectra shown in figures 5 and 10. Figure 13 also suggests that the linear regression line through the cloud of experimental data could be used to normalise the data underlying figure 10 without introducing a systematic error. Although this evaluation method hardly changed the obtained values for the activation energies, we did not apply it because of the weak foundation of this regression line.

Before presenting an explanation for the lack of concentration quenching demonstrated in figure 12, we first need to turn our attention to the spectra recorded from the annealed NDs at various Eu^{3+} concentrations. These spectra are presented in figure 14.

From the peak heights at 611.3 nm in figure 14 it can be concluded that the annealed NDs manifest concentration quenching that deviates strongly from the behaviour of non-annealed NDs, presented in figure 12. In fact, the concentration quenching shown in figure 14 is more similar to the behaviour in bulk cubic Y_2O_3:Eu^{3+} [27].

From the SAXS analyses presented in figure 3 and the background image of figure 3(a), we have determined that the thickness of the NDs is 0.9 nm, while the spacing between NDs on top of each other is 3.8 nm for the dried powder. The spacer consisting of oleic acid molecules prevents energy transfer from one ND to another, because the critical distance for energy transfer from one Eu^{3+} ion to a neighbouring Eu^{3+} ion is 1.7 nm in cubic Y_2O_3 [33]. This implies that the NDs with the stabilising oleic acid monolayer may be considered as isolated particles without exchange of energy between them. In fact, the oleic acid is diluting the Y_2O_3:Eu^{3+} material

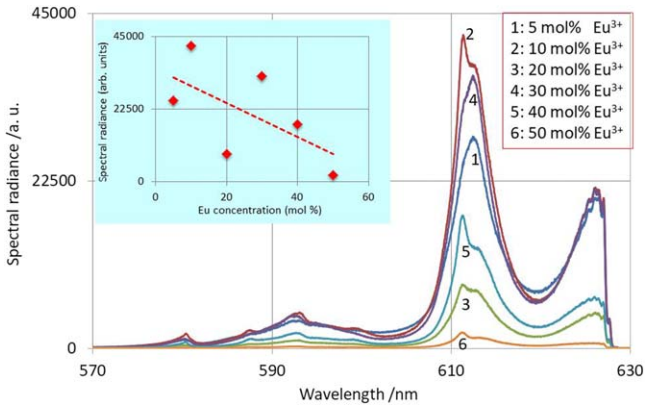

Figure 14. LA-spectra of Y_2O_3:Eu^{3+} NDs annealed at 500 °C. All spectra were recorded at 25 °C. The inset shows the spectral radiance of the peak at 611.3 nm. The dashed line in the inset is a linear regression.

and lowering the packing density of Y_2O_3:Eu^{3+} material with a factor of $3.8/0.9 = 4.2$. Ignoring the Eu–Eu distances inside the NDs for a moment and assuming that the density of the NDs is equal to that of bulk material, it is to be expected that concentration quenching of a cluster on NDs sets in at 4.2 times larger concentrations than in bulk material. This would explain the results presented in figure 12, while a further implication of this reasoning would be that the efficiency of the NDs cannot be larger than that of bulk material. As mentioned above, the lumen efficacy measurements were not accurate enough to verify this idea: nevertheless, this hand-waving consideration cannot be true anyway, because we have ignored the distances between Eu-ions inside the NDs. What the low packing density of the non-annealed NDs is telling us, is that the intrinsic luminescence of the NDs is rather strong.

In the case of the annealed NDs the oleic acid monolayer has been burnt and the closest distance between two ND can be much less than 1.7 nm. In that case the NDs are no longer isolated and can exchange energy. This explains the results presented in figure 14: the concentration quenching depends on the packing density in the powder and the resulting closest distance between parallel oriented NDs. This is difficult to control experimentally and it explains the large variation of the spectral radiance in figure 14. Although packing density arguments should not be ignored in experiments with nano-sized materials, they cannot explain the results of figure 12. Concentration quenching is radiationless energy transfer from an excited Eu^{3+} level to the Y_2O_3 lattice through both the proximity of neighbouring Eu^{3+} ions and phonon interaction. We found in the Raman spectra of the Y_2O_3:Eu^{3+} NDs hardly any lattice vibrations, so we conclude that the PDOS is largely reduced in the NDs. This will result in less radiationless losses and hence, it explains qualitatively the reduction of the concentration quenching in extremely thin NDs of Y_2O_3:Eu^{3+}. This idea has not been considered in the treatment of electron–phonon interaction described by Chen *et al* [7].

However, it must be stated that there is an alternative possibility to explain the lack of concentration quenching in the non-annealed NDs. This is based on the fact that the Y_2O_3:Eu^{3+} NDs contain at the most three layers of metal atoms and likely only one or two layers. A Eu^{3+} cation in an excited state, emitting its energy in the form of visible light, can in theory do this over in any direction from its outer 'surface'. Since most of these directions are not in the plane of the ND, then this may account for such little quenching. This explanation is based on the geometry of the NDs that only present Eu^{3+} neighbouring cations in specific directions rather than all directions as found in bulk solids.

Unfortunately, the spectroscopic data obtained in the present investigations do not give sufficient relevant information to substantiate the hypotheses on reduced electron–phonon interaction and the geometry of the ultrathin NDs. More theoretical work is needed to obtain a full understanding of the lack of concentration quenching in the NCs.

3.2. Structural characterisation of the Eu doped NDs

The physical properties of these nanomaterials can be elucidated through an assessment of their atomic scale structure (i.e. their spatial distribution/arrangement and their associated binding energies). Their structural characterisation must be carefully investigated, especially when dealing with ultra-small dimensions. The ultra-small size regime, situated at the lower end of the nanoscale (i.e. around 1 nm), appears to be a regime in transition between the molecular scale (e.g. clusters) and the conventional nanoscale [34]. We posit that one of the most important effects in ultra-small nanostructures is the notable modification of the atomic structure due to the change in surface energy, stabilising ligand effects, and the presence of defects and strains. All of these phenomena must be taken into account to ascertain the relationships between the crystal structure and physical properties of a given ultra-small NC. The fact that NCs are usually characterised by classical x-ray powder diffraction does not necessarily mean that the technique is well suited to all situations [35]. In the ideal case, a crystal is described as being constructed from identical unit cells, which are repeated an infinite number of times within three-dimensional space. Although a real crystal is always a finite object, the infinite periodic lattice works very well because the number of unit cells inside a small micron-size crystal (e.g. 10–100 μm) is still several orders of magnitude larger than the number of unit cells that constitute its surface. The behaviour of charge carriers, photons, phonons, and others can be assessed in a 'bulk' environment in which surface effects can be reasonably neglected (at least in a diffraction experiment). Yet, when at least one-dimension of a crystal is comparable to the size of a unit cell (i.e. the ultra-small size regime), reconsidering the infinite periodic lattice and the associated induced consequences from a crystallographic point of view (e.g. broken symmetry) is more than legitimate [36].

The as-prepared ultrathin europium-doped yttrium oxide NDs constitute a perfect model system for this because their thickness (0.9 ± 0.2 nm) is as small as the cubic (space group Ia-3, #206) unit cell of 'bulk' Y_2O_3 ($a = 10.6$ Å). All well-defined (i.e. individual NCs with narrow size and shape

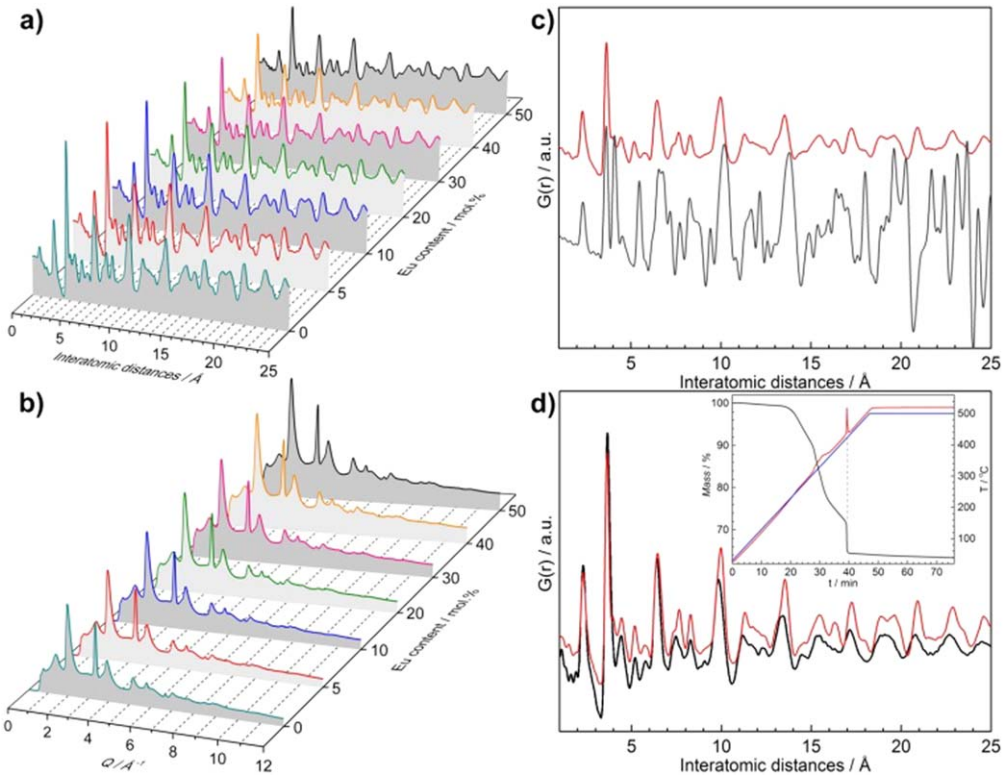

Figure 15. (a) Experimental atomic pair distribution function (PDF-G(r)) data and (b) wide angle x-ray scattering patterns of ultrathin europium-doped (0, 5, 10, 20, 30, 40 and 50 mol%) yttrium oxide nanodiscs (NDs). (c) Example of the PDF modelling of the bulk cubic structure (space group Ia-3) of yttrium oxide (dark grey) compared with the experimental PDF obtained for ultrathin europium-doped (5 mol%) yttrium oxide NDs (red). (d) Juxtaposition of the PDF data of the as-prepared europium-doped (5 mol%) yttrium oxide NDs (red) and the NDs after thermal treatment at 500 °C for 30 min (black). The inset in (d) shows the thermal treatment (blue: thermal profile, red: sample temperature, right scale) performed on europium-doped (5 mol%) yttrium oxide NDs and the corresponding thermogravimetric analysis (left scale).

distributions) europium-doped yttrium oxide NCs reported in the literature are characterised by at least one ultra-small dimension (≈10 Å). Although the reported structural data often are insufficient or are in contrast with other presented experimental data, such as photoluminescence (PL) spectra (see discussion above), the crystal structure of ultra-small europium-doped yttrium oxide NCs have been identified as either 'bulk' cubic [13] (space group Ia-3) or monoclinic [12] (space group C2/m, #12) structures.

Interestingly, the most commonly used argument to explain the discrepancies between the experimental data and the proffered interpretation stemming from the 'bulk' hypothesis is related to 'surface effects'. Hence, such a situation leads to a scientific conundrum from which surface effects are simultaneously strong enough to explain the modification of the physical properties (i.e. PL properties in the case of europium-doped yttrium oxide NCs) and negligible when considering the crystal structure. The main consequence is a lack of clarity in unravelling the relationship between optical properties and crystal structure.

The experimental PDF (G(r)) (see ESI for details of the PDF measurements) and classical WAXS data, obtained for the as-prepared ultrathin europium-doped yttrium oxide NDs, are shown in figures 15(a) and (b), respectively. The PDF approach accounts for diffuse scattering (i.e. total scattering experiments including both Bragg and diffuse scattering) whereas the WAXS approach only considers Bragg scattering [37].

The two data sets reveal that, independent of the europium content (i.e. from 0 mol% up to 50 mol%), all prepared samples are isostructural. Indeed, the peaks positions, peaks shapes, and their relative intensities match as a function of the europium content. The only noticeable difference is that the peaks are shifted towards longer distances (figures 15(a) and S4(a)) or shorter Q values (figures 15(b) and S4(b)) as functions of increasing europium content from 0 mol% up to 50 mol%. Such a phenomenon is expected for the formation of real solid solutions (i.e. no phase separation) because of the slight difference of the ionic radii of Y^{3+} (0.89 Å) and Eu^{3+} (0.95 Å). In other words, substituting Y^{3+} by larger cations, such as Eu^{3+}, will contribute to increased interatomic distances. A second point is that the PDF data obtained for ultrathin europium-doped yttrium oxide NDs differ from the data recently reported for ultrathin europium oxide nanoplatelets [20].

While the corresponding 'bulk' materials are isostructural, ultra-small NCs are not. Adding more than 50 mol% of europium prevents the formation of well-defined NDs, yielding a mixture of different shapes (figure S5). Further, 'bulk' cubic (space group Ia-3) or monoclinic (space

group C2/m) structures do not map well the PDF of ultrathin europium-doped yttrium oxide NDs (figures 15(c) and S6). Indeed, when comparing the PDFs of ultrathin europium-doped yttrium oxide NDs and bulk bcc Y_2O_3 (figure 15(c)), obvious differences are observed.

In the light of the discussion on the spectroscopic results it is not surprising that the structure of the NDs does not fit with bulk cubic or bulk monoclinic Y_2O_3. Indeed more evidence (from FTIR measurements) for the structures of the NDs before and after annealing being different in agreement with our earlier arguments is presented below.

The FTIR analyses clearly show that all samples are protected by oleate anions (figure S7). As a consequence, the outermost layers must be made of Y^{3+}/Eu^{3+} ions. The negatively charged layers made of carboxylate anions from the oleate ligands stabilise the NDs and allow the maintenance of the electric neutrality within the unit cell. The coordination of the carboxylate anions to the Y^{3+}/Eu^{3+} layers is also constrained by the arrangement of the C18 alkyl chains (steric hindrance, coulombic interactions, van der Walls forces). As a consequence, the coordination and bond distances of 'inner' and 'outer' oxygen atoms are most likely different, and two distinct types of oxygen atoms should be defined, in contrast with the case for the bulk bcc structure. Finally, because of the ultra-small thickness of the NDs, the probable existence of two different types of oxygen atoms, and modified Y–Y distances, both the overall bcc symmetry and cationic sites symmetry are not likely to have been maintained (broken symmetry). These simple crystallographic considerations constitute a plausible alternative to the recently given structural interpretations based on the formation of 'bulk' structures [12, 13].

Annealing the europium-doped yttrium oxide NDs at high temperature (500 °C–30 min) under oxidising conditions (O_2) facilitates the removal of the majority of the ligands. The corresponding TGA (figure 15(d), inset) indicates that 36 wt% of the mass of the sample consisted of oleate anions, clearly indicating that the as-prepared NDs are more appropriately described as an inorganic-organic hybrid material instead of a purely inorganic material with a thin organic surfactant (because of the ultra-small thickness). Interestingly, the PDF analysis of the annealed sample (figure 15(d)), although similar to that of the as-prepared sample, clearly shows differences. Not only are the peaks shifted to smaller interatomic distances, but they also are broader. The broadening of the peaks indicates the formation of a more disordered system, which is unexpected because high temperature annealing treatments are typically used to improve the crystallinity of inorganic materials. Interestingly, such behaviour might be explained by considering the organic ligand and, particularly, the carboxylate moieties, as components of the structure that stabilised a metastable. Unfortunately, the crystal structure of these ultrathin NDs has not yet been solved. Methods to solve the atomic arrangement of such nanostructures, one that is equivalent to the techniques to solve 'bulk' materials, is still extremely complicated [38–40]. Creating a structural model from scratch is highly challenging and requires PDF data that is coupled to additional local probes (e.g. EXAFS); these are needed to progress forward.

4. Conclusions

From the work presented in this article various conclusions can be drawn. The first is that the presented NDs of Y_2O_3:Eu^{3+} with a thickness of about 1 nm can be fabricated in a reproducible, facile and self-assembling process, which does not depend on the Eu concentration. From the work of Si *et al* [13] it is known that many NDs with the generic composition of Ln_2O_3 and Y_2O_3:Ln can be synthesised according to this method. We expect that our results will stimulate others to assess and modify these NDs, before they can beneficially be used in biological probes.

The second conclusion refers to the change of the spectra and the lack of concentration quenching of the NDs. Laser-activated spectra of luminescent materials often yield a wealth of data from which far-reaching conclusions can be derived. This is also the case for the study presented in this article. Hence, the obvious second conclusion is that the crystal field in the Y_2O_3:Eu^{3+} NDs deviates clearly from that in bulk cubic and monoclinic Y_2O_3:Eu^{3+} phosphors, albeit the shape of the $^5D_0 \rightarrow {}^7F_J$ ($J = 0, 1, 2$) transitions shows some similarity with the monoclinic transitions. The very small thickness of the NDs also causes a substantial broadening of the Eu^{3+} transition lines. This indicates that the Eu^{3+} ions sit in positions with slightly different crystal field, depending on the distance to the surface of ND. This surface-related effect is assumed to be important in all NC-rare-earth-doped phosphors.

The Raman spectra of the non-annealed NDs manifest various vibration modes of the oleic acid molecules, which are used to synthesise and stabilise the NDs; moreover, the Raman spectra surprisingly indicate that the NDs show hardly any vibrational modes that can be assigned to Y_2O_3. This inference leads to the final hypothesis of this work: the largely suppressed concentration quenching of the Eu^{3+} luminescence of the NDs is related to the reduction of vibrational modes of the NDs, which may indicate a weak electron–phonon interaction. More work will be necessary to substantiate this idea.

Acknowledgments

We are grateful to the EPSRC and Technology Strategy Board (TSB) for funding the PURPOSE (TP11/MFE/6/1/AA129F; EP-SRC TS/G000271/1) and CONVERTED (JeS no. TS/1003053/1), PRISM (EP/N508974/1) and FAB3D programs. We are finally grateful to the TSB for funding the CONVERT program.

This research was supported by the National Science Foundation (NSF) Award CHE-1402298. Research was carried out in part at the Center for Functional Nanomaterials, Brookhaven National Laboratory, which is supported by the US Department of Energy, Office of Basic Energy Sciences, under Contract No. DE-SC0012704. Use of the National Synchrotron Light Source II, Brookhaven National Laboratory, is supported by the US Department of Energy, Office of Science, Office of Basic Energy Sciences, under Contract No.

DE-SC0012704. Elementary chemical analyses (ICP-AES) were performed at the Dartmouth College Trace Element Analysis Core, which is partially supported by NIEHS P42 ES007373, NIEHS P01 ES022832, EPA RD83544201.

ORCID iDs

T G Ireland https://orcid.org/0000-0001-6512-9540
J H Dickerson https://orcid.org/0000-0001-9636-6303

References

[1] Gai S, Li C, Yang P and Lin J 2014 *Chem. Rev.* **114** 2343–89
[2] Chen G, Yang C and Prasad P N 2013 *Acc. Chem. Res.* **46** 1474–86
[3] Liu G 2015 *Chem. Soc. Rev.* **44** 1635–52
[4] Bera D, Quan L and Holloway P H 2008 Phosphor quantum dots *Luminescent Materials And Applications* ed A Kitai (Chichester: Wiley) ch 2, pp 19–73
[5] Silver J and Withnall R 2008 Color conversion phosphors for LEDs *Luminescent Materials and Applications* ed A Kitai (Chichester: Wiley) ch 3, pp 75–109
[6] Liu G K and Chen X 2007 Spectroscopy of lanthanide nanophosphors *Frontier Developments in Optics and Spectroscopy* ed B Di Bartolo and O Forte (Boston, MA: Boston College)
[7] Chen X Y, Zhuang H Z, Liu G K, Li S and Niedbala R S 2003 *J. Appl. Phys.* **94** 5559–65
[8] Wang H, Uehara M, Nakamura H, Miyazaki M and Maeda H 2005 *Adv. Mater.* **17** 2506–9
[9] Zhang W-W, Zhang W-P, Xie P-B, Yin M, Chen H-T, Jing L, Zhang Y-S, Lou L-R and Xia S-D 2003 *J. Colloid Interface Sci.* **262** 588–93
[10] Bazzi R *et al* 2004 *J. Colloid Interface Sci.* **273** 191–7
[11] Bazzi R, Flores-Gonzalez M A, Louis C, Lebbou K, Dujardin C, Brenier A, Zhang W, Tillement O, Bernstein E and Perriat P 2003 *J. Lumin.* **102–103** 445–50
[12] Pinna N, Garnweitner G, Beato P, Niederberger M and Antonietti M 2005 *Small* **1** 112–21
[13] Si R, Zhang Y W, Zhou H P, Sun L D and Yan C H 2007 *Chem. Mater.* **19** 18–27
[14] Som S and Sharma S K 2012 *J. Phys. D: Appl. Phys.* **45** 415102
[15] Bipin Kumar G, Haranath D, Shikha S, Singh V N and Shanker V 2010 *Nanotechnology* **21** 055607
[16] Zhao D, Se S, Zhang H, Bae B S and Qin W P 2010 *J. Nanosci. Nanotechnol.* **10** 2036–9
[17] Bihari B, Eilers H and Tissue B M 1997 *J. Lumin.* **75** 1–10
[18] Eilers H and Tissue B M 1996 *Chem. Phys. Lett.* **251** 74–8
[19] Park J, Joo J, Kwon S G, Jang Y and Hyeon T 2007 *Angew. Chem., Int. Ed. Engl.* **46** 4630–60
[20] Hudry D, Abeykoon A M M, Hoy J, Sfeir M Y, Stach E A and Dickerson J H 2015 *Chem. Mater.* **27** 965–74
[21] Ilavsky J and Jemian P R 2009 *J. Appl. Crystallogr.* **42** 347–53
[22] Ding Y, Gu J, Ke J, Zhang Y-W and Yan C-H 2011 *Angew. Chem., Int. Ed. Engl.* **50** 12330–4
[23] den Engelsen D and de Koning B 1974 *J. Chem. Soc. Faraday Trans.* I **70** 1603–14
[24] Son J S, Park K, Kwon S G, Yang J, Choi M K, Kim J, Yu J H, Joo J and Hyeon T 2012 *Small* **8** 2394–402
[25] Li Z and Peng X 2011 *J. Am. Chem. Soc.* **133** 6578–86
[26] Liu Y H, Wang F, Wang Y, Gibbons P C and Buhro W E 2011 *J. Am. Chem. Soc.* **133** 17005–13
[27] Buijs M, Meijerink A and Blasse G 1987 *J. Lumin.* **37** 9–20
[28] Silver J, Martinez-Rubio M I, Ireland T G, Fern G R and Withnall R 2001 *J. Phys. Chem.* B **105** 9107–12
[29] Leavitt R P, Gruber J B, Chang N C and Morrison C A 1982 *J. Chem. Phys.* **76** 4775–88
[30] den Engelsen D, Ireland T G, Harris P G, Fern G R, Reip P and Silver J 2016 *J. Mater. Chem.* C **4** 8930–8
[31] Williams D K, Bihari B, Tissue B M and McHale J M 1998 *J. Phys. Chem.* B **102** 916–20
[32] den Engelsen D, Fern G R, Ireland T G and Silver J 2018 *J. Lumin.* **196** 337–46
[33] den Engelsen D, Harris P, Ireland T and Silver J 2015 *ECS J. Solid State Sci. Technol.* **4** R1–9
[34] Hu S and Wang X 2012 *Sci. China Chem.* **55** 2257–71
[35] Palosz B, Grzanka E, Gierlotka S and Stel'Makh S 2010 *Z. Kristallogr.* **225** 588–98
[36] Palosz B, Grzanka E, Gierlotka S, Stel'Makh S, Pielaszek R, Bismayer U, Neuefeind J, Weber H P and Palosz W 2002 *Acta Phys. Pol.* A **102** 57–82
[37] Petkov V 2008 *Mater. Today* **11** 28–38
[38] Juhás P, Cherba D M, Duxbury P M, Punch W F and Billinge S J L 2006 *Nature* **440** 655–8
[39] Doan-Nguyen V V T, Kimber S A J, Pontoni D, Reifsnyder Hickey D, Diroll B T, Yang X, Miglierini M, Murray C B and Billinge S J L 2014 *ACS Nano* **8** 6163–70
[40] Yang X, Masadeh A S, McBride J R, Bozin E S, Rosenthal S J and Billinge S J L 2013 *Phys. Chem. Chem. Phys.* **15** 8480–6